Quadrature nonreciprocity: unidirectional bosonic transmission without breaking time-reversal symmetry

Clara C. Wanjura,[1,*] Jesse J. Slim,[2,*] Javier del Pino,[3,2] Matteo Brunelli,[4] Ewold Verhagen,[2,†] and Andreas Nunnenkamp[5,‡]

[1] *Cavendish Laboratory, University of Cambridge, Cambridge CB3 0HE, United Kingdom*
[2] *Center for Nanophotonics, AMOLF, Science Park 104, 1098 XG Amsterdam, The Netherlands*
[3] *Institute for Theoretical Physics, ETH Zürich, 8093 Zürich, Switzerland*
[4] *Department of Physics, University of Basel, Klingelbergstrasse 82, 4056 Basel, Switzerland*
[5] *Faculty of Physics, University of Vienna, Boltzmanngasse 5, 1090 Vienna, Austria*

Nonreciprocity means that the transmission of a signal depends on its direction of propagation. Despite vastly different platforms and underlying working principles, the realisations of nonreciprocal transport in linear, time-independent systems rely on Aharonov-Bohm interference among several pathways and require breaking time-reversal symmetry. Here we extend the notion of nonreciprocity to unidirectional bosonic transport in systems with a time-reversal symmetric Hamiltonian by exploiting interference between beamsplitter (excitation preserving) and two-mode-squeezing (excitation non-preserving) interactions. In contrast to standard nonreciprocity, this unidirectional transport manifests when the mode quadratures are resolved with respect to an external reference phase. Hence we dub this phenomenon *quadrature nonreciprocity*. First, we experimentally demonstrate it in the minimal system of two coupled nanomechanical modes orchestrated by optomechanical interactions. Next, we develop a theoretical framework to characterise the class of networks exhibiting quadrature nonreciprocity based on features of their particle-hole graphs. In addition to unidirectionality, these networks can exhibit an even-odd pairing between collective quadratures, which we confirm experimentally in a four-mode system, and an exponential end-to-end gain in the case of arrays of cavities. Our work opens up new avenues for signal routing and quantum-limited amplification in bosonic systems.

In nonreciprocal systems, e.g. isolators, the transmission varies when interchanging input and output, in an ideal case from unity to zero [1–4]. Nonreciprocity is a resource for many applications, including sensing [5], constructing bosonic networks with general routing capabilities [6], and realising topological phases [7]. Complemented with gain, nonreciprocity amplifies weak signals while protecting the source against noise, making it ideal for quantum information processing applications [8]. Magnetic-free isolators and directional amplifiers have been proposed based on parametric modulation [3, 9, 10], interfering parametric processes [11, 12], and reservoir engineering [13] and were experimentally demonstrated in different platforms, e.g. superconducting circuits [14–16] and optomechanical systems [17–24].

In linear systems, achieving nonreciprocal response relies on breaking time-reversal symmetry (TRS) in the Hamiltonian by employing real or synthetic magnetic fields and dissipation. The directionality in this standard kind of nonreciprocity (sNR) does not depend on the phase of the input signal. In this work we extend the notion of nonreciprocity in linear bosonic systems by identifying a class of systems that show a kind of unidirectional signal transmission, positioned between reciprocal and standard nonreciprocal transmission, whose (uni)directionality depends on the phase of the input signal. We dub the defining property of this class quadrature nonreciprocity (qNR), as it can be revealed when resolving the signal into its quadrature components. In contrast to sNR, a qNR Hamiltonian does not break TRS, but achieves unidirectional transport by interfering beamsplitter (excitation-preserving) and two-mode squeezing (excitation non-preserving) interactions. It does not require strong Kerr nonlinearity [3, 25, 26] or spin-polarized emitters [27, 28]. We report experimental realisations using an optomechanical network and construct a comprehensive theoretical framework exposing an entire class of qNR systems with exciting properties, including an even-odd pairing between collective quadratures and exponential end-to-end gain in resonator chains. Our work introduces systematic tools to treat unidirectional phase-sensitive transport in bosonic lattice, which have recently sparked interest in connection with bosonic analogues of the Kitaev chain [29–31]. It further opens the door to studying exotic phenomena in these models, such as multi-mode entanglement [29] and non-Hermitian topology [32]. From the point of view of applications, the concept of qNR opens up new avenues for signal routing and amplification.

Defining quadrature nonreciprocity (qNR)

We consider a network of N driven-dissipative bosonic modes. Their steady-state response to a coherent probe follows from the Heisenberg-Langevin equations of motion $\dot{\mathbf{q}} = \mathcal{M}\mathbf{q} - \sqrt{\gamma}\mathbf{q}_{\text{in}}$ for the field quadratures $x_j \equiv (a_j +$

* C. C. W. and J. J. S. contributed equally to this work.
† verhagen@amolf.nl
‡ andreas.nunnenkamp@univie.ac.at

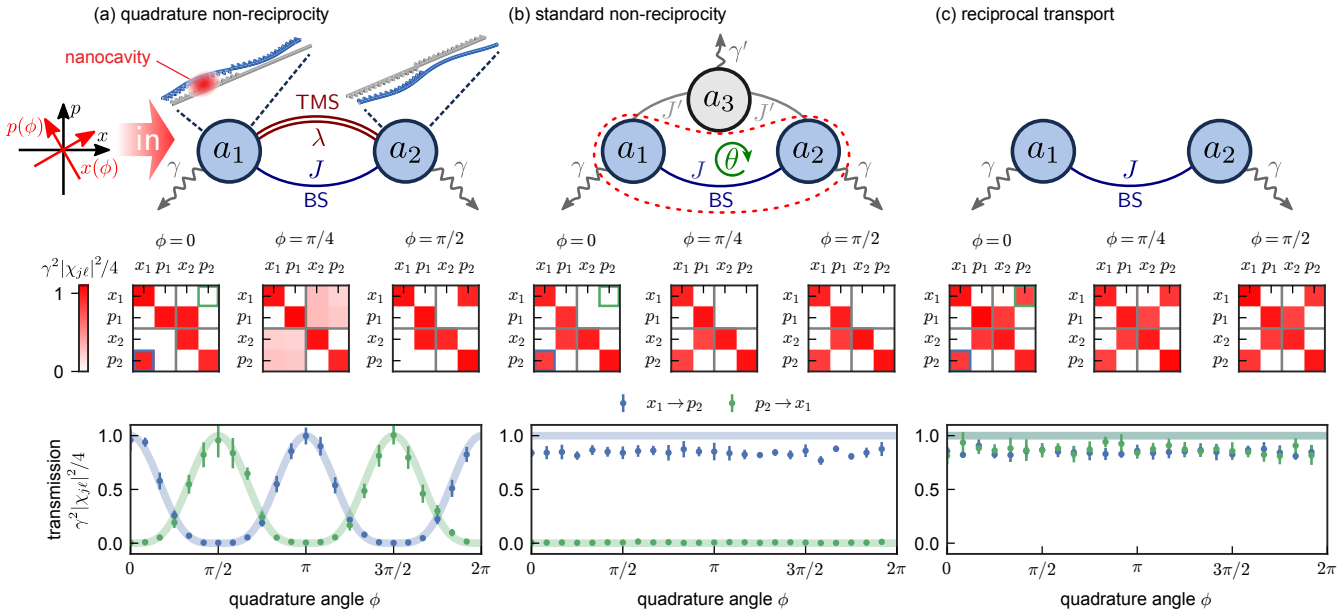

FIG. 1. **Quadrature nonreciprocity (qNR) vs. standard nonreciprocity (sNR) vs. reciprocal transport.** Coupled-mode diagrams for three systems that feature distinct forms of transport, realized in an experiment with mechanical modes $a_{1,2}$ (equal decay rate $\gamma = 2\pi \times 3.7$ kHz) subject to optomechanically-mediated beamsplitter (BS, strength J) and two-mode squeezing (TMS, strength λ) interactions. Panel (a) includes a sketch of the spatial profiles for the mechanical modes coupled to the experimental optical nanocavity. Coherent excitation along quadratures (red) rotated by ϕ from the reference gauge (black) is sketched (first row). Corresponding measured susceptibility matrix amplitudes evolve differently with ϕ (middle row). Nonreciprocity manifests in an asymmetric modulus of the susceptibility matrix $|\chi| \neq |\chi|^{\mathrm{T}}$. The behaviour of the elements within the green and blue boxes shows whether reciprocity can be tuned by the incoming quadrature angle (bottom row). (a) Two modes interact through BS and TMS of equal strength ($J = \lambda = \gamma/4$), showing qNR. Nonreciprocity vanishes for $\phi = \pi/4$. Furthermore, setting $\phi = \pi/2$ inverts the transmission direction. (b) An auxiliary mechanical mode a_3 (decay rate $\gamma' = 2\pi \times 1.3$ kHz) is coupled to $a_{1,2}$ through BS interactions of strength $J' = \sqrt{\gamma\gamma'}/2$, providing a coupling between a_1 and a_2 via a_3 that can interfere with the direct coupling $J = \gamma/2$. SNR requires the breaking of TRS – realized by picking a non-trivial phase $\theta = \pi/2$ along both paths, akin to a synthetic flux – so that the susceptibility matrix is nonreciprocal for all ϕ. Regardless of the hierarchy of loss rates $\gamma \lessgtr \gamma'$, perfect isolation can be attained (Supplementary Information Sec. IB). (c) Reciprocal transport between two modes coupled only through BS ($J = \gamma/2$) is characterised by a symmetric susceptibility matrix for any phase ϕ. Error bars are obtained by repeating the measurement sweep 10 times and represent the statistical $\pm 2\sigma$ spread around the average value.

$a_j^\dagger)/\sqrt{2}$ and $p_j \equiv -\mathrm{i}(a_j - a_j^\dagger)/\sqrt{2}$, where a_j denotes the annihilation operator for the bosonic mode $j \in (1, \cdots, N)$, $\mathcal{M}$ the dynamical matrix and γ the damping rate. We use the vector notation $\mathbf{q} \equiv (x_1, p_1, \cdots, x_N, p_N)^{\mathrm{T}}$ for the system's quadratures and similarly $\mathbf{q}_{\mathrm{in}}$ for the quadrature inputs. We assume that each mode dissipates only via coupling to the input-output port, although our analysis extends to general temporal coupled-mode theory [19, 33]. The scattering matrix $S(\omega)$ connects input $\mathbf{q}_{\mathrm{in}}$ and output quadratures $\mathbf{q}_{\mathrm{out}}$ with frequency ω, satisfying the input-output boundary conditions $\mathbf{q}_{\mathrm{out}} = \mathbf{q}_{\mathrm{in}} + \sqrt{\gamma}\mathbf{q}$ [34, 35]. Namely,

$$S(\omega) \equiv \mathbb{1} + \gamma(\mathrm{i}\omega\mathbb{1} + \mathcal{M})^{-1} \equiv \mathbb{1} + \gamma\chi(\omega), \qquad (1)$$

with the susceptibility matrix $\chi(\omega) \equiv (\mathrm{i}\omega\mathbb{1} + \mathcal{M})^{-1}$. We will from now on consider resonant driving ($\omega = 0$ in a frame rotating at the mode frequencies) and write $\chi \equiv \chi(0)$, $S \equiv S(0)$ for brevity.

Let us consider a rotation of each quadrature pair $\{x_j, p_j\}$ with respect to some external phase reference, see Fig. 1 (a) inset, namely

$$\begin{pmatrix} x_j(\phi_j) \\ p_j(\phi_j) \end{pmatrix} = \begin{pmatrix} \cos\phi_j & \sin\phi_j \\ -\sin\phi_j & \cos\phi_j \end{pmatrix} \begin{pmatrix} x_j(0) \\ p_j(0) \end{pmatrix} \equiv R(\phi_j) \begin{pmatrix} x_j(0) \\ p_j(0) \end{pmatrix}. \qquad (2)$$

Equation (2) can be understood as a $U(1)$ gauge transformation in the mode basis $\{a_j, a_j^\dagger\}$ [15, 20] (Supplementary Information Sec. IIA). The susceptibility matrix χ transforms as

$$\chi_\phi \equiv U(\phi_j)\chi U^{\mathrm{T}}(\phi_j), \qquad (3)$$

where we introduced $U(\phi_j) \equiv \oplus_{j=1}^{N} R(\phi_j)$.

Nonreciprocity is typically defined by asymmetric transmission amplitudes [1, 3]. We adopt this notion in a generalised sense, with signals split into their x, p quadratures, meaning $|S|^{\mathrm{T}} \neq |S|$ for Eq. (1) or, equivalently, $|\chi|^{\mathrm{T}} \neq |\chi|$ ($|\cdots|$ denotes taking the element-wise modulus). We say a

system exhibits quadrature nonreciprocity (qNR) if there exist at least *two* different sets of local gauges $\phi_j^{(1,2)}$ corresponding to a nonreciprocal and reciprocal susceptibility matrix, respectively. Mathematically, this implies a pair of rotations $U_{1,2} \equiv \oplus_{j=1}^{N} R(\phi_j^{(1,2)})$ such that

$$|U_1 \chi U_1^{\mathrm{T}}|^{\mathrm{T}} \neq |U_1 \chi U_1^{\mathrm{T}}| \text{ and } |U_2 \chi U_2^{\mathrm{T}}|^{\mathrm{T}} = |U_2 \chi U_2^{\mathrm{T}}|. \quad (4)$$

qNR dimer: the simplest qNR system

We now introduce the minimal system displaying qNR: the parametrically-driven dimer shown in Fig. 1 (a). It comprises two modes $a_{1,2}$ coupled via beamsplitter (BS) coupling of strength J and two-mode-squeezing (TMS) coupling of strength λ. In a frame rotating at the mode frequencies, the Hamiltonian reads

$$H = J a_1^\dagger a_2 + \lambda a_1^\dagger a_2^\dagger + \text{H.c.} \quad (5)$$

corresponding to the most general bi-linear coupling. As we explain below, we implement these couplings between mechanical resonators through a time-modulated optical spring. For $J = \lambda$, we recover the well-known position-position coupling, which has been extensively studied, e.g. for implementing quantum non-demolition measurements [36, 37] or generating squeezing and entanglement [38]. Moreover, this Hamiltonian was also introduced as bi-directional phase-sensitive amplifier in [39] which was implemented in a superconducting circuit and used for qubit readout [40], and considered as starting point for nonreciprocity with broken time-reversal symmetry in [13].

As we now show, this coupling has important impact in the context of nonreciprocal signal transduction. Eq. (5) gives the following equations of motion for the quadratures

$$\begin{aligned}
\dot{x}_1 &= -\frac{\gamma}{2} x_1 + (J-\lambda) p_2 - \sqrt{\gamma} x_{1,\mathrm{in}}, \\
\dot{p}_1 &= -\frac{\gamma}{2} p_1 - (J+\lambda) x_2 - \sqrt{\gamma} p_{1,\mathrm{in}}, \\
\dot{x}_2 &= -\frac{\gamma}{2} x_2 + (J-\lambda) p_1 - \sqrt{\gamma} x_{2,\mathrm{in}}, \\
\dot{p}_2 &= -\frac{\gamma}{2} p_2 - (J+\lambda) x_1 - \sqrt{\gamma} p_{2,\mathrm{in}}, \quad (6)
\end{aligned}$$

from which we can see that the quadratures can decouple, due to the fact that BS and TMS couplings enter with opposite sign. In particular, setting $J = \lambda$ in Eq. (6) leads to perfect decoupling between $\dot{x}_1$ ($\dot{x}_2$) and p_2 (p_1), while $\dot{p}_2$ ($\dot{p}_1$) still couples to x_1 (x_2), in a way which is formally equivalent to a cascaded quantum system [41, 42]. This is also reflected in the susceptibility matrix

$$\chi = \begin{pmatrix} -\frac{2}{\gamma} & 0 & 0 & 0 \\ 0 & -\frac{2}{\gamma} & \frac{8J}{\gamma^2} & 0 \\ 0 & 0 & -\frac{2}{\gamma} & 0 \\ \frac{8J}{\gamma^2} & 0 & 0 & -\frac{2}{\gamma} \end{pmatrix}. \quad (7)$$

We interpret this property by saying that a signal encoded in quadrature x_1 can propagate from mode 1 to 2, emerging as p_2, while the reverse transduction, i.e., $p_2 \to x_1$ does not take place. When $J = \lambda > \gamma/4$, we further have $S_{x_2 \to p_1} = \gamma \chi_{x_2 \to p_1} > 1$, which signifies phase-sensitive amplification.

To demonstrate this unidirectional transport between quadratures, we implement Hamiltonian (5) in a sliced photonic crystal nanobeam – a nano-optomechanical network where multiple non-degenerate, MHz-frequency flexural mechanical modes are coupled to a single broad-band, telecom-frequency optical mode via radiation pressure. Two mechanical modes with equal linewidth γ serve as resonators a_j, with effective interactions enabled via the cavity by temporally modulated optical driving of a detuned laser. Specifically, BS (TMS) coupling is stimulated by modulating the intensity of the drive laser at the mechanical frequency difference (sum) [43], allowing control over both strength *and* phase of the interaction through depth and phase of the modulation tone, respectively (Methods). This particular protocol for parametric coupling between mechanical modes operates in the bad-cavity limit $\kappa \gg \omega_j$ and at large optical detuning $\Delta = -\kappa/(2\sqrt{3})$, with κ the cavity linewidth. Under these conditions, mechanical displacement modifies the intracavity photon number instantaneously on mechanical timescales. Through suitable drive laser intensity modulation, additional sidebands are created in the optical force that are mutually resonant between selected resonators (Methods). In effect, this protocol can implement arbitrary quadratic bosonic Hamiltonians for mechanical resonators [44].

In addition, the optomechanical interaction allows optical read-out of the nanobeam displacement, as imprinted on the intensity of a spectrally-resolved probe laser reflected from the cavity. The detected displacement signal $h(t) = k_1 z_1(t) + k_2 z_2(t) + \ldots$ contains a superposition of the resonator coordinates $z_j(t)$, transduced with strengths k_j, which can be resolved in frequency as the resonators' frequency separation greatly exceeds their linewidths.

In our measurements, we define (electronic) local oscillators (LOs) at the resonator frequencies ω_j that demodulate – in parallel – the displacement signal, to obtain the amplitude envelope $|a_j(t)|$ and relative phase $\varphi_j(t)$ of each resonator's harmonic motion $z_j(t) = |a_j(t)| \cos(\omega_j t + \varphi_j(t))$. In effect, the LOs *define* a rotating frame of reference in which the resonator dynamics can be tracked by a complex amplitude $\langle a_j \rangle = |a_j| e^{i\varphi_j}$, or equivalently by the quadrature amplitudes $\langle x_j \rangle = \sqrt{2}\,\mathrm{Re}(\langle a_j \rangle)$ and $\langle p_j \rangle = \sqrt{2}\,\mathrm{Im}(\langle a_j \rangle)$. Finally, signals to drive the resonator quadratures coherently through radiation pressure are derived from the same LOs, turning our experiment into a lock-in measurement. A sketch of the set-up is shown in Extended Data Fig. 2.

To connect the unidirectional response of Eq. (7) to the definition of qNR (4), we need to study how the dimer transforms under a change of gauge. We measure the dimer's quadrature-resolved response, when performing the gauge transformation in Eq. (3) (see Fig. 1 (a) inset).

This is experimentally achieved by referring both the interaction tones and LOs to a common time origin and subsequently adding a phase offset ϕ to the LOs, rotating the quadratures they define. Note that even though the frequencies of LOs ($\omega_{1,2}$) and interaction tones ($\omega_1 \pm \omega_2$) are all distinct, the fact that the latter signals can be derived from the former through mixing leads to a well-defined relation between the LO and interaction phases (Methods).

For different phases ϕ, we independently reconstruct the susceptibility matrix (3) for $J = \lambda$ in Fig. 1 (a). For the full expression of (3) we refer to Supplementary Information Sec. I.A, here we focus on the matrix elements shown in the bottom row of Fig. 1, namely

$$\chi_{x_1 \to p_2} = \frac{8J\cos^2(\phi)}{\gamma^2}, \tag{8}$$

$$\chi_{p_2 \to x_1} = -\frac{8J\sin^2(\phi)}{\gamma^2}. \tag{9}$$

It is clear that nonreciprocity only reveals itself in particular rotated quadratures. While maximal nonreciprocity is obtained for $\phi = 0$, as in Eq. (7), a gauge transformation reduces the 'contrast' of the nonreciprocity until, at $\phi = \pi/4$, the transport is completely reciprocal, i.e., $\chi_{x_1 \to p_2} = \chi_{p_2 \to x_1} = 4J/\gamma^2$, and in fact $|\chi|^{\mathrm{T}} = |\chi|$. This confirms that the dimer is indeed a qNR system, as per our definition (4). Further increasing ϕ swaps the direction of nonreciprocity, $a_1 \leftrightarrow a_2$, with complete reversal at $\phi = \frac{\pi}{2}$, when $\chi_{x_1 \to p_2} = 0$, $\chi_{p_2 \to x_1} = 8J/\gamma^2$.

In the qNR dimer, the cancellation at $\phi = \pi/4$ and the reversal of directionality fundamentally stems from TRS. We identify a system's TRS from its Hamiltonian, i.e. its dynamics in absence of local dissipation or gain. This is motivated by the fact that dissipation or gain by themselves, while breaking TRS in a 'trivial' way, cannot induce nonreciprocal behaviour. In Supplementary Information Sec. IIB-D we demonstrate that TRS implies the constraints $|\chi_{x_j \to x_\ell}| = |\chi_{p_\ell \to p_j}|$, $|\chi_{x_j \to p_\ell}| = |\chi_{x_\ell \to p_j}|$ for any gauges ϕ_j and reciprocity for at least one set of gauges. This is strikingly different from a system that breaks TRS, such as the isolator of Ref. [13]. In Fig. 1 (b) we show the measured susceptibility matrix for the 'sNR isolator', which is implemented in our optomechanical system from two equal-linewidth mechanical modes a_1 and a_2, coupled directly via a BS interaction of strength J while an auxiliary lower-order mechanical mode a_3 is introduced and coupled to both a_1 and a_2 with BS strength J'. Contrary to the qNR dimer, here isolation is enabled by a $U(1)$ gauge-invariant flux θ, the relative phase between the couplings J, J' as shown in Fig. 1 (b). Since nonreciprocity is controlled by the TRS-breaking flux, it is independent of local rotations in phase space by ϕ, as reflected by the phase-independent susceptibility matrices in Fig. 1 (b) ($|\chi_{x_1 \to x_2}|^2 = |\chi_{p_1 \to p_2}|^2 = 1$, $|\chi_{x_2 \to x_1}|^2 = |\chi_{p_2 \to p_1}|^2 = 0$).

For reference, we also contrast both notions of nonreciprocity against a reciprocal system. We display in Fig. 1 (c) the susceptibility matrix measured for two beamsplitter-coupled modes, which is completely reciprocal ($|\chi|^{\mathrm{T}} = |\chi|$) and gauge-invariant ($\chi_\phi = \chi$).

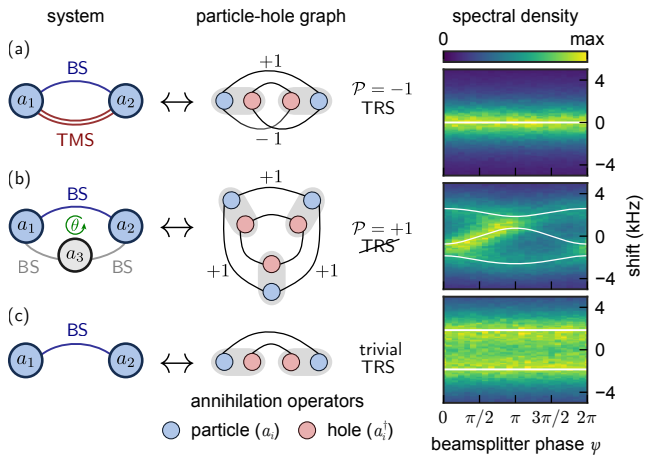

FIG. 2. **Time-reversal symmetry and qNR.** The coupled-mode diagrams (left column) of the systems studied in Fig. 1 are expanded using a general graph representation of quadratic Hamiltonians (middle column). Operators a_j, a_ℓ, $a_j^\dagger$, $a_\ell^\dagger$, annihilating 'particles' and 'holes' respectively, that are coupled in the equations of motions are connected through a line. (a) If the graph forms a double loop as is the case for the qNR dimer, TRS is always preserved. (b) If the resulting graph decomposes into two loops as for the sNR isolator, TRS can be broken by a gauge invariant phase, enabling sNR. (c) When the graph displays no loops as is the case for the trivial BS dimer, TRS is always preserved. The spectral density of the thermal fluctuations in mode a_1 serves as an experimental signature of TRS (right column). In a gauge where all other interactions are real, we vary the phase ψ of the BS coupling between a_1 and a_2. For (a) and (c), this does not affect the system's eigenfrequencies, given by the real part of the dynamical matrix' eigenvalues (white lines), while for (b) it signals TRS breaking. Experimental parameters are identical to those used in Fig. 1.

Time-reversal symmetry and qNR

The results above point to the fact that preserving TRS in the Hamiltonian is a key element, which sets qNR apart from sNR. A time-reversal symmetric Hamiltonian imposes certain symmetries on the dynamical matrix that underlie the unique transformation properties of a qNR susceptibility matrix. This motivates us to provide a general characterisation of TRS Hamiltonians in bosonic networks. TRS means that there exists a $U(1)$ transformation

$$a_j \to e^{\mathrm{i}\phi_j} a_j, \tag{10}$$

that renders the coefficients in the Hamiltonian real [45]. In concrete experiments, that realise the Hamiltonian terms through parametric driving, finding the phases ϕ_j in Eq. (10) that lead to a real Hamiltonian is equivalent

to making the time-dependent parametric drives symmetric in time ($t \to -t$). As we see here, even though there is one gauge in which the drive is symmetric in time, systems with phase-dependent transmission can feature unidirectional transmission. While TRS is often associated with reciprocity [3], TRS *only* requires $|\chi|$ to be symmetric for one set of phases $\phi_j^{(0)}$ in Eq. (10), see Supplementary Information Sec. II.B. Indeed, in qNR systems, reciprocity *only* occurs when $\phi_j = \phi_j^{(0)}$ (in the qNR dimer, $\phi_j^{(0)} = \phi^{(0)} = \pi/4, 3\pi/4$) and nonreciprocity occurs for all $\phi_j \neq \phi^{(0)}$. This feature, which to the best of our knowledge has not been recognised before, positions qNR precisely between reciprocity and gauge-independent sNR.

We develop a criterion to identify TRS for arbitrary quadratic bosonic Hamiltonians, based on the graph representation of the Hamiltonian matrix in the field basis, inspired by Bogoliubov-de-Gennes theory [44], see Supplementary Information II.B. We associate the Hamiltonian matrix with a graph in which the ladder operators a_j—annihilating 'particle' excitations—and $a_j^\dagger$—annihilating 'hole' excitations—are represented as vertices and the interactions as edges, i.e., connecting a_j to a_ℓ (and $a_j^\dagger$ to $a_\ell^\dagger$) for BS between sites j, ℓ and a_j to $a_\ell^\dagger$ (and $a_j^\dagger$ to a_ℓ) for TMS. The graph representations of the three systems of Fig. 1 display manifestly different structures (Fig. 2), leading to a general criterion for TRS (Supplementary Information Sec. III). The graph of the qNR dimer, Fig. 2 (a), connects all vertices in a *double* loop visiting each site twice. Such double loops guarantee TRS for arbitrary, complex, coupling constants. In contrast, the graph of the sNR isolator, Fig. 2 (b), decomposes into two disjoint loops. This structure allows to break TRS through a non-vanishing relative phase between the coupling constants. The BS dimer, Fig. 2 (c), displays no loops and trivially preserves TRS.

The different graph structures, which embody the behaviour under time reversal, are catalogued in general by a $\mathbb{Z}_2$ invariant, which we call *loop product* $\mathcal{P}$. To define such a quantity, we consider the particle-hole graph for a general loop with BS and TMS interactions. Then by multiplying by (-1) for a line crossing (TMS coupling) and $(+1)$ for an uncrossed pair of lines (BS couplings), the loop product $\mathcal{P}$ distinguishes between an even (disjoint loops) and odd number (double loop) of line crossings

$$\mathcal{P} \equiv (-1)^{n_{\mathrm{TMS}}}(+1)^{n_{\mathrm{BS}}} = \begin{cases} -1: & \text{double loop (TRS)} \\ +1: & \text{disjoint loops} \end{cases}, \tag{11}$$

with n_{BS} the number of BS couplings and n_{TMS} the number of TMS couplings. Eq. (11) indicates that the only requirement for TRS in a general loop is an odd number of TMS couplings, i.e. their position in the loop is irrelevant.

Complementing our graph-based theoretical criterion above, the experimental response of a system to incoherent excitation serves as a signature of a TRS Hamiltonian [44] as nontrivial fluxes manifest in the eigenfrequencies (Fig. 2 (right column)). We choose a gauge in which all interactions are real, except for the BS coupling between modes a_1 and a_2 present in all three systems studied so far, whose phase ψ we vary. Thermal fluctuations drive stochastically all mechanical quadratures homogeneously and lead to a power spectrum insensitive to ψ if there is a gauge transformation (10) that removes this BS phase. In our experiment this indicates the TRS of the qNR (Fig. 2 (a)) and BS Hamiltonians (Fig. 2 (c)). Conversely, if the eigenfrequencies tune with ψ, such a gauge transformation cannot exist, marking the broken TRS of the sNR isolator (Fig. 2 (b)).

Finally, we stress another consequence of TRS, already visible in the dimer (see Eq. (9)), i.e., that quadratures travel in pairs in opposite directions. In fact, the transduction $x_j \to p_\ell$ is accompanied by $x_\ell \to p_j$ with equal transmission in the opposite direction, e.g., in Eq. (7), $|\chi_{x_j \to p_\ell}|^2 = |\chi_{x_\ell \to p_j}|^2$, see the Supplementary Information Sec. IIC-D for the proof. This requirement of counter-propagating pairs of quadratures is reminiscent of other TRS systems, such as quantum spin Hall systems [7, 46].

Constructing qNR ring networks

We now take inspiration from the particle-hole graphs and look for qNR in TRS-preserving N-mode ring networks ($\mathcal{P} = -1$), dubbed 'N-rings' from now on. To obtain a ring with qNR transmission, a TRS Hamiltonian is only necessary, not sufficient. We also have to guarantee that BS and TMS couplings can interfere. The particle-hole representation allows a reinterpretation of the quadrature decoupling condition discussed along with Eq. (6) as constructive and destructive interference between particle-conserving and particle non-conserving processes. This condition brings us to the necessary and sufficient criterion for qNR. Besides the odd number of TMS couplings (Eq. (11)), achieving qNR requires that the ring consists of an *even* number of modes. To understand why, we take a closer look at the 4-mode ring with a single TMS interaction (Fig. 3 (a)). The corresponding equations of motion for equal couplings ($J = \lambda$) read

$$\begin{aligned} \dot{x}_1 &= -J(p_2 - p_4) - \frac{\gamma}{2}x_1 - \sqrt{\gamma}x_{1,\mathrm{in}} \\ \dot{p}_2 - \dot{p}_4 &= -\frac{\gamma}{2}(p_2 - p_4) - \sqrt{\gamma}(p_{2,\mathrm{in}} - p_{4,\mathrm{in}}). \end{aligned} \tag{12}$$

The coupling to x_1 vanishes in the second equation for the collective quadrature $(p_2 - p_4)$ due to the interference of BS and TMS couplings. Equations (12) have a similar structure as those for the qNR dimer (6), the main difference being that x_1 couples nonreciprocally to the *collective* quadrature $(p_2 - p_4)$ instead of to a local quadrature. Analogously, x_2 couples to $(p_1 - p_3)$ nonreciprocally. As a consequence, the dominant elements of the susceptibility matrix are coupling $(p_1 - p_3)$ to $-x_2$ and x_4, as well as $(p_2 - p_4)$ to $-x_1$ and x_3. This peculiar

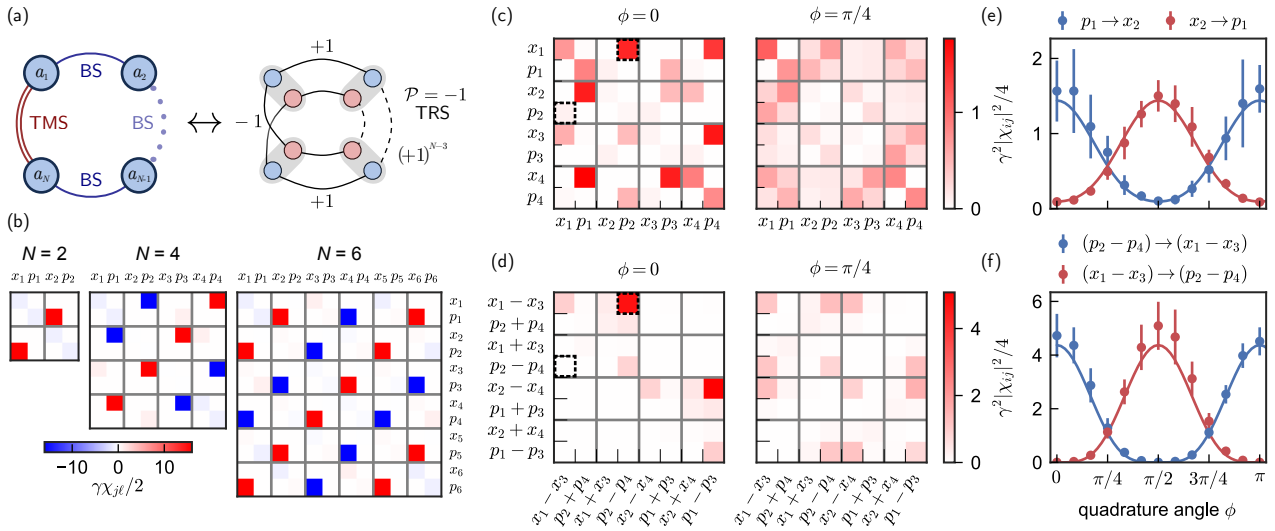

FIG. 3. **qNR transmission in ring networks.** (a) Graph representation of a ring with N modes, featuring a single TMS interaction. The ring is closed by $N-1$ BS interactions between the remaining modes. For arbitrary N the loop product $\mathcal{P}=-1$, indicating preservation of TRS. To obtain qNR transmission, N must be even. (b) A feature of qNR that only becomes apparent for $N>2$ is the pairing between collective quadratures of even and odd sites in the susceptibility matrix χ, shown here in theory for $J=\lambda=2N\cdot\gamma$ and $\phi=0$. (c) Susceptibility matrices $|\chi|$ for the $N=4$ ring realized in experiment. We equalize all resonator dampings to $\gamma=2\pi\times 10$ kHz using feedback (Methods) and set $J=\lambda=2\pi\times 5$ kHz, the largest λ that permits a linear response to thermal noise in the experiment. For $\phi=0$, we obtain a nonreciprocal χ that shows collective pairing, albeit with reduced contrast compared to (b). For $\phi=\pi/4$, χ is reciprocal, showing the qNR of transmission of the ring. (d) Susceptibility matrices in the basis of even and odd collective quadratures show their pairing for $\phi=0$, when χ is block-diagonal. Similarly, reciprocal susceptibility is obtained for $\phi=\pi/4$. (e,f) The values of selected susceptibility matrix elements (e: resonator basis; dashed boxes in c, f: collective basis; dashed boxes in d) show continuous tuning as function of quadrature angle ϕ, in theory (solid line) and experiment (circles). Even in theory, the isolation for $\phi=0,\pi/2,\pi$ in the resonator basis (e) is not perfect, whereas in the collective basis (f) it is. Error bars are obtained by repeating the measurement sweep 10 times and represent the statistical $\pm 2\sigma$ spread around the average value.

non-local pairing between even and odd quadratures is shown in Fig. 3 (b) for a 4-ring and carries over to larger N-rings with even N, independent of system size. The pairing is only possible if N is even, since it requires an equal number of quadratures on even and odd sites, respectively. We rigorously derive this condition using the particle-hole graphs and a reduction technique detailed in Supplementary Information Sec. IV.

We implement the 4-ring shown in Fig. 3 (a) experimentally. The measured susceptibility matrix in the resonator quadrature basis, (Fig. 3 (c)) illustrates its nonreciprocal response for $\phi=0$, while the nonreciprocity vanishes completely for $\phi=\pi/4$, establishing qNR in this system. For maximum nonreciprocity ($\phi=0$), the largest magnitude entries of the susceptibility matrix instantiates the non-local coupling structure between quadratures of even and odd sites. This susceptibility matrix structure is transparent in the basis of collective quadratures (Fig. 3 (d)), where χ is, in fact, block-diagonal for $\phi=0$. We note that in this basis the nonreciprocal isolation is perfect in theory (Fig. 3f), whereas in the local basis it is not (Fig. 3e).

Towards qNR lattices

Going one step further, we use qNR rings as building blocks for constructing qNR lattices. It follows from Supplementary Information Sec. IIC and IV that if a lattice overall preserves TRS and contains at least one qNR ring, it is itself qNR.

Of particular interest are translational-invariant chains of qNR N-rings, which can combine qNR transmission with non-Hermitian topology [32]. One such example is given by the bosonic Kitaev chain of Ref. [29], which corresponds to a 2-ring chain with a specific choice of inter-ring coupling phases and is indeed a qNR system. Thanks to our particle-hole graph framework, we can now consider more complex scenarios. As an example, we take a chain of qNR 4-rings connected through BS interactions. In Figs. 4 (a) and (b), we show the simulated steady-state field quadratures for this qNR lattice for $\phi=0$, given a quadrature-resolved input at different sites. Nonreciprocal transmission is clearly visible, while changing the gauge to $\phi=\pi/4$ (not shown), leads to complete reciprocity, i.e., we recover the characteristic feature of qNR, Eq. (4). The pairing we characterised in the previous sections also manifests: an input at the $p_{1,1}$ quadrature (in which the

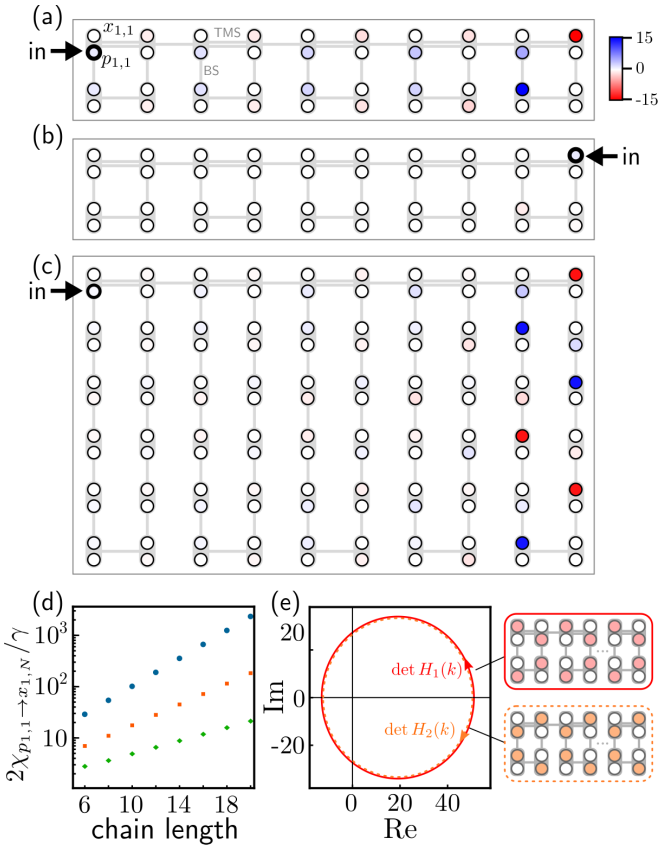

FIG. 4. **Steady-state response of a qNR chain.** Staggering qNR rings with BS links to form a chain, we obtain a qNR system for which the largest steady-state response is at the opposite end. We show the numerically calculated steady-state field quadratures $\langle x_{j,l}\rangle/(2\sqrt{\gamma}\langle x_{\mathrm{ss};j,l}\rangle)$, $\langle p_{j,l}\rangle/(2\sqrt{\gamma}\langle p_{\mathrm{ss};j,l}\rangle)$ (of the site in row j, column ℓ) for (a)-(b) a 4-ring qNR chain driven at the (a) first and (b) last site; and (c) a 12-ring qNR chain. The pairing is clearly visible in the steady state response. (d) End-to-end gain for 4-ring (blue), 8-ring (red) and 12-ring (green) chains and $J = \lambda = 4\gamma$. The gain grows exponentially across the system and with system size. (e) Suggested non-Hermitian topological invariant exploiting the Block-diagonal form of the Fourier-transformed dynamical matrix with blocks $\mathcal{M}_{1,2}(k)$ (Methods).

indices stand for row and column in the array), Fig. 4 (a), procures the largest steady-state response at two sites at the opposite end of the chain. The pairing is evidenced in larger qNR ring sizes, in which the steady-state response of an 8-ring chain is most prominent in every second site of the last plaquette shaping a zig-zag line (Fig. 4 (c)).

In this system, qNR is accompanied by amplification with the end-to-end gain growing exponentially with the chain length, see Fig. 4 (d). This generalises the phase-dependent directional amplification predicted in a bosonic Kitaev chain [29]. Directional amplification with exponential end-to-end gain has been identified as proxy of non-trivial topology [32, 47]. Based on previous results for 2-ring chains, we conjecture a connection with a non-trivial non-Hermitian winding number, calculated from the determinant of the non-Hermitian matrix [48], the dynamical matrix in our case (Methods). In Fig. 4 (e), we plot the determinant of each of the diagonal blocks of the Bloch-matrix (each of the blocks accounts for a set of collective quadratures, see Fig. 4 (e)) for the 4-ring qNR chain of Fig. 4 (a) under periodic boundary conditions. We find that the determinant of each of these blocks can be assigned a non-trivial winding number which equals in magnitude and differs in sign corresponding to the two directions of directional end-to-end gain. The opposite winding sense of these two matrix blocks is an expression of the TRS Hamiltonian.

Outlook

In conclusion, we introduced the novel phenomenon of quadrature nonreciprocity (qNR). In contrast to standard nonreciprocity, qNR does not break time-reversal symmetry in the Hamiltonian and presents a characteristic gauge dependence. We identified the set of bosonic networks that display qNR and reported the first experimental realisations.

Our results point to a close connection of qNR with the existence of QND variables and with back-action evading (BAE) measurements [36, 37]. Indeed, our characterisation of qNR simultaneously provides a powerful recipe to design systems with collective QND variables. In this context, exploring the noise properties of the qNR networks we introduced will also be interesting. As they rely on interference between coherent interactions, without necessity of dissipation, we can expect quantum-limited performance on suitable platforms [49]. Future qNR devices may play a part in quantum applications, such as efficient, noiseless sensors, quantum information routers and the generation and measurement of non-classical states, including entangled states [29, 35, 50, 51]. Indeed, while we demonstrated the concept in the domain of nanomechanics, it could find application in e.g. classical electrical circuits [52], acoustics [53], superconducting circuits [14–16], and spin ensembles [54].

Going forward, we envision the construction of lattices from qNR rings which inherit the qNR properties similar to those of Fig. 4 demonstrating the generality of our framework and relevance for other domains such as non-Hermitian topology. In the optomechanical realm, real and synthetic dimensions offer scaling potential, e.g. by assembling multiple nanobeams [43] or by addressing higher-order overtones. Moreover, it will be interesting to explore qNR Hamiltonians with other platforms that already demonstrated larger lattice sizes, such as Ref. [55]. Our research opens new avenues for exploring qNR lattices and networks in which new topological phenomena may emerge similar to the quantum spin Hall effect [7, 46].

Acknowledgements

We thank A. A. Clerk and D. Malz for useful discussions. C.C.W. acknowledges the funding received from the Winton Programme for the Physics of Sustainability and EPSRC (EP/R513180/1). J.d.P. acknowledges financial support from the ETH Fellowship program (grant no. 20-2 FEL-66). M.B. acknowledges funding from the Swiss National Science Foundation (PCEFP2_194268). This work is part of the research programme of the Netherlands Organisation for Scientific Research (NWO). It is supported by the European Union's Horizon 2020 research and innovation programme under grant agreement No 732894 (FET-Proactive HOT) and the European Research Council (ERC starting grant no. 759644-TOPP).

METHODS

Linear response and interference of beamsplitter and squeezing interactions

A general quadratic, bosonic Hamiltonian can be written in the field basis of creation and annihilation modes, namely $\{a_i, a_i^\dagger\}$, as

$$H = \sum_{i,j} \left(a_i^\dagger \mathcal{A}_{ij} a_j + \frac{1}{2}(a_i^\dagger \mathcal{B}_{ij} a_j^\dagger + a_i \mathcal{B}_{ij}^* a_j) \right), \quad (13)$$

where overall constant shifts have been removed. Here, the matrix elements $\mathcal{A}_{ij} = J_{ij} e^{-i\varphi_{ij}}$, $\mathcal{A}_{ji} = \mathcal{A}_{ij}^*$ of the Hermitian *hopping matrix* $\mathcal{A}$ encode beamsplitter interactions that conserve the total number of excitations. Similarly, we define the symmetric *squeezing matrix* $\mathcal{B}$ that encodes the particle-non-conserving squeezing interactions in its elements $\mathcal{B}_{ij} = \lambda_{ij} e^{i\theta_{ij}}$, $\mathcal{B}_{ji} = \mathcal{B}_{ij}$.

In the quadrature basis $x_j = (a_j + a_j^\dagger)/\sqrt{2}$ and $p_j = \mathrm{i}(a_j^\dagger - a_j)/\sqrt{2}$, Eq. (13) reads

$$H = \sum_{i,j} \left(T_{ij} p_i p_j + V_{ij} x_i x_j + U_{ij} x_i p_j + U_{ij}^T p_i x_j \right), \quad (14)$$

where we define the effective potential matrices $U = \mathrm{Im}(\mathcal{B} - \mathcal{A}), V = \mathrm{Re}(\mathcal{A} + \mathcal{B})$ and kinetic energy $T = \mathrm{Re}(\mathcal{A} - \mathcal{B})$ [56]. The corresponding Heisenberg equations of motion read

$$\begin{pmatrix} \dot{x}_j \\ \dot{p}_j \end{pmatrix} = \sum_{k=1}^{N} \begin{pmatrix} U_{kj} x_k + T_{jk} p_k \\ -V_{jk} x_k - U_{jk} p_k \end{pmatrix} - \begin{pmatrix} \gamma_j x_j \\ \gamma_j p_j \end{pmatrix}. \quad (15)$$

In our platform, quadratic Hamiltonians of the form Eq. (13) are effectively conceived in a rotating frame of reference that oscillates at the natural frequencies of the resonators. As such, free energy terms $\propto a_i^\dagger a_i$ are absent, and the matrix elements for U, V, T read

$$\begin{aligned} V_{ij}, T_{ij} =& J_{ij} \cos(\varphi_{ij}) \pm \lambda_{ij} \cos(\theta_{ij}), \\ U_{ij} =& \lambda_{ij} \sin(\theta_{ij}) + J_{ij} \sin(\varphi_{ij}). \end{aligned} \quad (16)$$

These expressions show that matching interaction amplitudes and complex interaction phases can lead to a cancellation of different contributions in Eq. (14), decoupling quadratures from different resonators in the dynamics governed by Eq. (15), see Ref. [29, 30]. This is the case for $\lambda_{ij} = J_{ij}$ and $\theta_{ij} = \varphi_{ij} = n\pi/2$, $n \in \mathbb{Z}$, where $T = V = 0$. This can be interpreted as destructive interference in the particle-hole space, see Ref. [44] and main text.

From the coefficients in Eq. (15), we define the dynamical matrix $\mathcal{M}$ for the quadrature vector $\mathbf{q} = (x_1, p_1, \ldots, x_N, p_N)^T$, as the matrix that fulfills $\dot{\mathbf{q}} = \mathcal{M}\mathbf{q} - \mathbf{f}^{(q)}$. Here $\mathbf{f}^{(q)}$ is a column vector grouping driving amplitudes for each quadrature. The quadrature response to excitation is determined by the matrices U, V and T through the susceptibility matrix

$$\chi(\omega) = (\mathrm{i}\omega \mathbb{1} + \mathcal{M})^{-1}. \quad (17)$$

On resonance (in the rotating frame, this is equivalent to $\omega = 0$), this matrix will present asymmetries if and only if $\mathcal{M}$ is a nonzero asymmetric matrix. A more exhaustive discussion is provided in Supplementary Information, Sec. IIB.

Device

The device, a suspended sliced photonic crystal nanobeam hosting a telecom-frequency optical mode coupled simultaneously to multiple non-degenerate flexural mechanical modes, was used in a previous study [44], where details can be found on its design and fabrication. For completeness, a micrograph along with the thermomechanical spectrum of the device is shown in Extended Data Fig. 1. The optical mode has a free-space wavelength $\lambda_0 \approx 1533.5$ nm and linewidth $\kappa \approx 2\pi \times 320$ GHz. The four mechanical modes ('resonators') we use have frequencies $\omega_j = 2\pi \times 3$–17 MHz, dissipation rates $\gamma_j = 2\pi \times 1$–4 kHz and photon-phonon coupling rates $g_{0,j} = 2\pi \times 3$–6 MHz.

Optically mediated mechanical interactions

The non-degenerate flexural nanobeam modes do not interact mechanically. However, by suitable modulation of radiation pressure backaction, cavity light can mediate controllable *effective* mechanical interactions [44, 57].

Our cavity operates in the unresolved sideband regime or bad-cavity limit ($\omega_j \ll \kappa$), such that external drives of the cavity field modulate the photon population n_c instantaneously on mechanical timescales. Moreover, for the optimal detuning $\Delta = -\kappa/(2\sqrt{3})$, mechanical displacements maximally modulate n_c and, in turn, the radiation pressure force that acts back on the displacement. For a single resonator, such instantaneous optomechanical backaction leads to the well-known optical spring effect [58], namely an effective shift $\delta\omega_j = 2g_j^2\Delta/(\Delta^2 + \kappa^2)$ in the resonator's frequency $\omega_j \mapsto \tilde{\omega}_j + \delta\omega_j$, where $\tilde{\omega}_j$ is the intrinsic mechanical frequency.

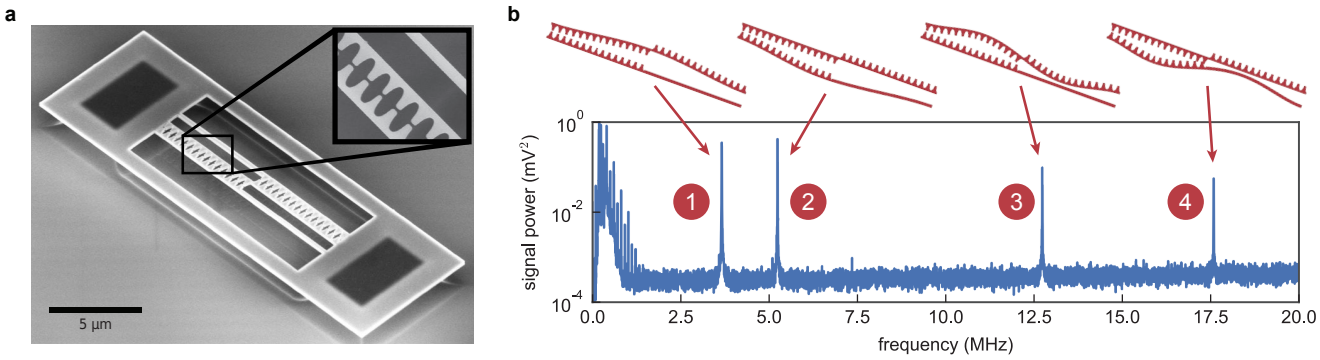

EXTENDED DATA FIG. 1. **Optomechanical device.** (a) Scanning electron micrograph of a device as used in our experiments. Three suspended beams are defined in the top silicon device layer (thickness 220 nm). The flexural motion of each pair of adjacent beams is coupled to an optical resonance, hosted by a point defect in the sliced photonic crystal defined by the teeth. In the presented experiments, we address only one of the cavities from free-space, at normal incidence, to drive and read out the mechanical motion of a single beam pair. The inset shows a top view, revealing the narrow slit separating the beam pair. More details can be found in [44]. (b) Spectrum of thermal fluctuations imprinted on the intensity of a read-out laser reflected off the optical cavity. In this frequency range, four mechanical resonances can be identified, with the corresponding simulated displacement profiles shown above. These mechanical modes serve as the resonators in the presented experiments.

In multimode systems, the cavity n_c contains contributions for each resonator's motion. For fixed drive laser intensity, contributions from different resonators are mutually off-resonant and only each resonator's self-backaction (i.e. optical spring) is relevant. However, a modulation of the drive laser intensity can cause the motion of one resonator to influence that of another one, by dynamically modulating the 'cross-resonator' optical spring. In practice, a harmonic modulation of the drive laser intensity with frequency ω_m, depth c_m and phase offset ϕ_m mixes with the displacement contributions in n_c to create additional sidebands in the optical force. By setting ω_m equal to a mechanical difference (sum) frequency $\omega_m = \omega_k - \omega_j$ ($\omega_m = \omega_k + \omega_j$), these sidebands are mutually resonant between resonators j and k. Consequently, by stimulating the resonant frequency conversion process selected by ω_m, these sidebands induce a light-mediated effective mechanical beamsplitter (squeezing) interaction after adiabatic elimination of the cavity field.

The effective beamsplitter and squeezing interaction rates J_{jk} and λ_{jk}, respectively, are tuned by the depth c_m of the corresponding modulation tone and given by [43, 44]

$$\{J_{jk}, \lambda_{jk}\} = c_m \frac{g_j g_k \Delta}{\Delta^2 + \kappa^2/4} = c_m \frac{\sqrt{\delta\omega_j \delta\omega_k}}{2}, \qquad (18)$$

where $g_j = \sqrt{\bar{n}_c} g_{0,j}$ is the optomechanical coupling rate enhanced by the laser-driven average cavity population $\bar{n}_c$. The last expression relates the interaction rates to the (easily measured) optical spring shifts $\delta\omega_j$, avoiding the need to know $g_{0,j}$ and the cavity in-coupling efficiency precisely. We note that $\delta\omega_i$ and $\delta\omega_j$ always have the same sign. Moreover, the modulation phase ϕ_m is imprinted on the effective interactions in the appropriate rotating frame (see section 'Phase coherent interaction tones') and controls time-reversal symmetry. Finally, as all mechanical frequencies are distinct and incommensurate, modulation tones can be applied simultaneously to induce multiple interactions.

Experimental set-up and procedures

In this study, we employed the same set-up as in [44], including the same procedures to characterise the system, to calibrate the experiments, and to attain phase coherence between driven and detected signals. For completeness, here we recapitulate those methods as presented in [44].

A schematic of the experimental setup is displayed in Extended Data Fig. 2. The nanobeam sample is placed in a vacuum chamber at room temperature and pressure $\sim 2 \times 10^{-6}$ mbar, aligned at 45° relative to the vertical polarisation light focused from free space at normal incidence. A detection laser (Toptica CTL 1550) far detuned from the cavity resonance ($\omega_{det} - \omega_c \approx -2.5\kappa$) at incident power $P_{det} = 2 - 4$ mW serves to detect the mechanical resonators' displacement. The detection laser light reflected from the cavity was filtered using a cross-polarised detection scheme, fibre coupled, separated from the other laser light using a tunable bandpass filter (DiCon), and detected on a fast photodetector (New Focus 1811, AC-coupled). Intensity modulations of the detection laser encoding resonator displacements were analysed using a Zurich Instruments UHFLI lock-in amplifier.

The intrinsic resonator frequencies $\tilde{\omega}_j$ and linewidths $\tilde{\gamma}_j$ were obtained from thermomechanical spectra, and vacuum optomechanical coupling rates $g_{0,j}/(2\pi) = \{5.30 \pm 0.14, 5.86 \pm 0.17, 3.29 \pm 0.30, 3.12 \pm 0.89\}$ MHz were estimated from nonlinear transduction [59] for the four resonators, respectively. The cavity linewidth was esti-

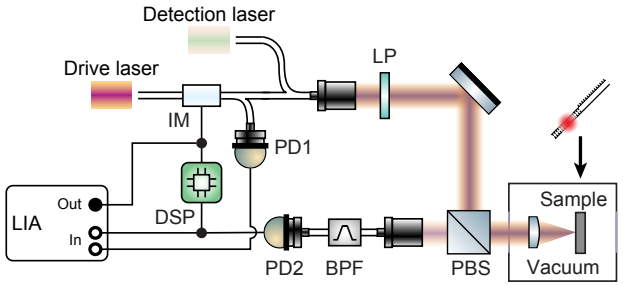

EXTENDED DATA FIG. 2. **Schematic of the experimental set-up.** A sample holding the sliced nanobeam device is placed in a room-temperature vacuum chamber rotated by 45° relative to the vertical polarization of the incoming light. Spectrally resolved drive and detection lasers are combined in-fibre, launched into free-space, and focused onto the sample, coupling into the nanocavity from normal incidence. In a cross-polarized detection scheme, the horizontal component of the light radiated out from the cavity is transmitted by a polarizing beamsplitter (PBS). Subsequently, a fibre-based tunable bandpass filter (BPF) rejects light at the drive laser frequency and transmits detection laser light onto a fast photodetector (PD2). A high-frequency lock-in amplifier (LIA) serves to analyze (In) the intensity modulations of the drive laser (for calibration) and detection laser, while also driving (Out) the drive laser intensity modulator (IM) through an amplification stage (not shown). In addition, the electronic displacement signal is routed through a digital signal processor (DSP) that optionally generates a feedback signal to modify resonator damping rates. LP, linear polarizer.

mated from the detuning dependence of the spring shift. A drive laser (Toptica CTL 1500) was launched through the same fibre and collimator into the setup after modulation by a Thorlabs LN81S-FC intensity modulator (IM) at incident power $P_{\mathrm{drive}} = 1.0$ mW. A small part of the modulated drive laser light was split off to be monitored by a fibre-coupled fast photodetector (New Focus 1811, DC-coupled).

Control signals, including sum- and difference-frequency tones to generate interactions as well as resonant excitation signals, were generated by the lock-in amplifier, amplified (Mini-Circuits ZHL-32A+ with 9 dB attenuation), and connected to the RF port of the IM to modulate the drive laser's radiation pressure.

Measurement-based feedback

Additionally, driving signals that regulate mechanical damping rates through measurement-based feedback were generated through filtering the electronic displacement signal using a digital signal processor (DSP, RedPitaya STEMlab 125-14) that implemented a configurable electronic bandpass filter with tunable gain and phase shift (using the PyRPL suite). The DSP output was combined with the control signals before the RF amplifier. Choosing a proper phase shift allows the effective feedback of a signal proportional to the mechanical velocity of a given resonator as a radiation pressure force to dampen the resonator, in an approach similar to [60, 61]. The desired damping rates are realised by adjusting the electronic feedback gain coefficients for each individual resonator. Further details on the procedure to calibrate the required electronic phase shifts and gains can be found in [44].

Characterisation and preparation of resonators

A standard procedure was performed immediately before every experiment to compensate for variations in in-coupling and out-coupling efficiency associated with drifts of the optical sample alignment: The spring-shifted resonator frequencies ω_j, linewidths γ_j, and root-mean-square (rms) displacement voltage levels $z_{\mathrm{rms},j}$ were obtained from thermomechanical spectra with modulations off. The displacement voltage corresponding to a single phonon amplitude was calculated using $z^2_{\mathrm{ph},j} = z^2_{\mathrm{rms},j}/(\bar{n}_j\tilde{\gamma}_j/\gamma_j)$. Here, $\bar{n}_j = k_B T/\hbar\omega_j$ is the thermal occupancy of the resonator's bath at $T = 295$ K and $\tilde{\gamma}_j/\gamma_j$ compensates for thermo-optically induced dynamical backaction [62].

This dynamical backaction is also actively controlled in the qNR dimer experiments to equalise the two resonators' loss rates, as an alternative to the measurement-based feedback described above: Fine-tuning the laser intensity allowed matching the linewidths of modes 3 and 4, as those exhibited different scaling with mean photon number.

Calibration of control signals

To induce effective interactions with desired rates λ_{jk}, J_{jk}, the required modulation depths c_{m} were determined from (18). For every individual tone, the DC-coupled modulation monitor detector was used to calibrate the relation between c_{m} and the electronic control signal amplitude V_{m}, compensating the frequency-dependent transmission of the RF chain.

The control tones are synthesized digitally by the lock-in amplifier. This allows to reference their phase offsets to an effective internal time origin, which then defines a deterministic gauge in which the modulation phases are set and the response is analysed.

Analysis of the displacement signal

As described in [44], the electronic displacement signal was demodulated in parallel at each resonator's frequency ω_i using electronic local oscillators internal to the lock-in amplifier that are referenced to the same clock as the control tones. For each resonator, the demodulated in-phase (I_i) and quadrature (Q_i) components were filtered (third-order low-pass filter, 3 dB bandwidth 50 kHz) and

combined into a complex amplitude $z_i(t) = I_i(t) + iQ_i(t)$ that is formally equivalent to the resonator amplitude in the rotating frame.

The total signal delay through the setup, from the LIA control outputs via the sample to the LIA input, was determined by driving each of the resonators and measuring the coherent response. The phase offset α_j between drive tone and coherent response of resonator j was extracted and fitted linearly against the resonator frequencies ω_j. The fitted delay (on the order of 100 ns) was used to relate the quadratures of the demodulated amplitudes $z_j(t)$ to those defined by the control tones.

Phase-coherent interaction tones

Even though the frequencies of LOs ($\omega_{j,\ell}$) and interaction tones ($\omega_j \pm \omega_\ell$) are all distinct, a phase relation between them can nevertheless be established. To do so, we absorb the explicit time dependence of each tone $\cos(\omega_k t + \varphi_k) = \cos\beta_k(t)$ into the instantaneous phase $\beta_k(t) = \omega_k t + \varphi_k$. Phase coherence is now attained between an interaction tone $j \pm \ell$ (at $\omega_j \pm \omega_\ell$) and the *combination* of both LOs j,ℓ ($\omega_{j,\ell}$), since the phase difference

$$\begin{aligned}\Delta\varphi_{j\pm\ell} &= \beta_{j\pm\ell}(t) - \big(\beta_j(t) \pm \beta_\ell(t)\big) \\ &= \varphi_{j\pm\ell} - (\varphi_j \pm \varphi_\ell) \end{aligned} \tag{19}$$

is stable (time-independent). Physically, this phase difference may be evaluated by generating a tone with the combined instantaneous phase $\beta_j(t) \pm \beta_\ell(t)$ through mixing of the LOs and subsequent high-pass (low-pass) filtering, and comparing that to the interaction tone.

Experimental settings

For the experiments shown in Figs.1 and 2, the mechanical resonances labeled 3 and 4 (frequencies $2\pi \times 12.8$ and $2\pi \times 17.6$ MHz) were used, with their decay rates matched thermo-optically to $\gamma = 2\pi \times 3.7$ kHz by appropriately adjusting the average drive laser intensity. For the three-mode experiments shown in Fig. 1b and Fig. 2b, the mechanical resonance labeled 2 (frequency $2\pi \times 5.3$ MHz, thermo-optically tuned dissipation rate $\gamma' = 2\pi \times 1.3$ kHz) is utilized as the auxiliary mode.

The four-mode experiments shown in Fig. 3 were performed using the mechanical resonances labelled 1 (frequency $2\pi \times 3.7$ MHz) through 4 at maximum drive laser power (thermo-optically tuned dissipation rates $2\pi \times \{1.9, 0.9, 4.2, 3.5\}$ kHz, respectively). In this case, simultaneous feedback cooling on all mechanical resonance was employed to increase and equalize their decay rates to $\gamma = 2\pi \times 10$ kHz. In addition to homogenizing the system, the feedback cooling reduces the amplitude of thermal fluctuations, thereby ensuring that the cavity photon population responds linearly to mechanical displacement and rendering non-linear transduction [59] and non-linear reduction of the optical spring shift unimportant.

Reconstructing the susceptibility matrices

The central relation used to analyse the results of our experiments is the steady-state response $\mathbf{q}_{\rm ss}$ of a system of N resonators described by Hamiltonian (13) to resonant forces driving its quadratures with amplitudes $\mathbf{f}^{(q)} = (f^{(q)}_{x_1}, f^{(q)}_{p_1}, \ldots, f^{(q)}_{x_N}, f^{(q)}_{p_N})^T$. This response is measured in units of the zero-point fluctuations $x_{{\rm zpf},j}$ and given by

$$\mathbf{q}_{\rm ss} = \chi_\phi(0)\mathbf{f}^{(q)}. \tag{20}$$

Harmonic driving forces are generated by modulation of the drive laser intensity $I(t) = I_0(1 + c_d\cos(\omega_d t + \phi_d))$, where I_0 is the average drive laser intensity, c_d the depth of the modulation, ω_d its frequency, matched to the mechanical resonance of interest, and ϕ_d its phase. Due to the short photon lifetime ($\kappa^{-1} \ll \omega_j^{-1}, \omega_d^{-1}$), the cavity population $n_c(t) \propto I(t)$ responds instantaneously to the drive laser intensity on the mechanical timescale, as do the resulting optical forces $F_j(t) = \hbar g_{0,j} n_c(t)/x_{{\rm zpf},j}$ on each resonator j. Although all mechanical resonators are coupled to the same cavity and thus experience similar optical forces, their large frequency separation ($|\omega_j - \omega_\ell| \ll \gamma_j, \gamma_\ell$) ensures that only a single mode is resonantly driven, allowing to neglect the driving on the other resonators.

The drive forces the evolution $\dot{\mathbf{a}} = \mathcal{M}^{(a)}\mathbf{a} - \mathbf{f}^{(a)}(t)$ of the mode vector $\mathbf{a} = (a_1, a_1^\dagger, \ldots, a_N, a_N^\dagger)^T$ (expressed in the frame rotating along with the resonators) through the driving vector $\mathbf{f}^{(a)}(t)$, with dynamical matrix $\mathcal{M}^{(a)}$ as defined in Supplementary Information Sec. IIB. The odd-index elements $f^{(a)}_{2j-1}(t) = {\rm i}e^{{\rm i}\omega_j t}F_j(t)/(2m\omega_j x_{{\rm zpf},j})$ encode the force $F_j(t)$ driving operator a_j, whereas the even-index elements $f^{(q)}_{2j}(t) = \left(f^{(q)}_{2j-1}(t)\right)^*$ are related by conjugation and drive the adjoint operator $a_j^\dagger$. For a driving force $F_j(t) = h_j\cos(\omega_j t + \phi_j)$ resonant with resonator j, with phase ϕ_j, the rotating factor $e^{{\rm i}\omega_j t}$ selects the positive frequency sideband of $F_j(t)$. We neglect the non-resonant negative frequency sideband in a similar spirit to the rotating-wave approximation. This results in time-independent driving terms

$$f^{(a)}_{2j-1} = {\rm i}\frac{h_j e^{-{\rm i}\phi_j}}{4m\omega_j x_{{\rm zpf},j}}. \tag{21}$$

Before each experiment we perform a driven reference measurement for each resonator to quantify how the modulation depth c_d is transduced into the driving term $f^{(a)}_{2j-1}$. We disable all interaction modulations, such that the dynamical matrix is diagonal and only contains damping terms ($\mathcal{M}^{(a)} \mapsto -\Gamma/2$). We then apply a modulation of depth between $c_d = 1$–$5 \cdot 10^{-3}$ and sweep its frequency ω_d across the resonance frequency ω_j of resonator j. We normalise the response to the zero-point

fluctuation amplitude, fit it with resonator susceptibility to obtain the driven amplitude $a_{\max}$ on resonance ($\omega_d = \omega_j$) and determine the force transduction coefficient $K_j = |f^{(a)}_{2j-1}|/c_d = a_{\max}\gamma_j/(2c_d)$.

To reconstruct the on-resonance susceptibility matrix $\chi_\phi(0)$ for a given quadrature angle ϕ, we first refer all (electronic) interaction and LO tones to a common time origin at which their phases are zero. Then, we shift the LO tone phases by ϕ to rotate the quadratures they define. We turn on the modulations that generate the desired interactions, and perform a series of $2N$ experiments where we drive the quadratures one by one, with $\arg(f^{(a)}_{2j-1}) = 0$ to drive x_j and $\arg(f^{(a)}_{2j-1}) = \pi/2$ to drive p_j for each resonator j while the terms driving the other resonators are zero. For each of these driving conditions $\mathbf{f}^{(a)}_k$, we record the steady state response amplitudes $\mathbf{a}_{\mathrm{ss},k}$ after averaging with a low-pass filter (third-order filter, 3 dB bandwidth $2\pi \times 10$ Hz).

We collect the driving vectors in the matrix $\mathcal{F}^{(a)} = \left[\mathbf{f}^{(a)}_1 \cdots \mathbf{f}^{(a)}_{2N}\right]$ and the steady-state responses in $A^{(a)} = [\mathbf{a}_{\mathrm{ss},1} \cdots \mathbf{a}_{\mathrm{ss},2N}]$. Next we transform to the quadrature basis via a matrix W, and obtain the real driving matrix $\mathcal{F}^{(q)} = W\mathcal{F}^{(a)} = \left[\mathbf{f}^{(q)}_1 \cdots \mathbf{f}^{(q)}_{2N}\right]$ that contains the quadrature driving amplitudes for each setting. Similarly, the real matrix $A^{(q)} = WA^{(a)} = \left[\mathbf{q}_{\mathrm{ss},1} \cdots \mathbf{q}_{\mathrm{ss},2N}\right]$ contains the steady-state responses in the quadrature basis. Noting that the columns of $\mathcal{F}^{(q)}$ span the entire driving space (and are in fact diagonal), equation (20) can be used to obtain the susceptibility matrix $\chi_\phi(0) = A^{(q)}(\mathcal{F}^{(q)})^{-1}$.

To estimate experimental errors, the full ϕ sweep from 0 to 2π was repeated 10 times. The matrix colour plots in Figs. 1 and 3 show average values over all sweeps, whereas the plots of single matrix elements feature error bars that represent the statistical $\pm 2\sigma$ (i.e. a 95% confidence interval) spread around the average value.

Non-Hermitian topological invariant

To analyse the topological properties of the chain shown in the main text Fig. 4, we write the dynamical equations for the quadratures under periodic boundary conditions, $J = \lambda$, and obtain the dynamical matrix in the plane-wave basis. We label the sites of each unit cell A_j for odd columns with $j \in \{1, 2\}$ the row index, and B_j for even columns. The resulting dynamical equations decouple into two respectively closed sets of equations for the sets of quadratures $\{x_j^{A_1}, x_j^{B_2}, p_j^{B_1}, p_j^{A_2}\}$, namely,

$$\begin{aligned}
\dot{x}_j^{A_1} &= -\frac{\gamma}{2}x_j^{A_1} + Jp_j^{A_2} - Jp_j^{B_1} + Jp_{j-1}^{B_1} - \sqrt{\gamma}x_{j,\mathrm{in}}^{A_1},\\
\dot{x}_j^{B_2} &= -\frac{\gamma}{2}x_j^{B_2} + Jp_j^{A_2} - Jp_j^{B_1} - \sqrt{\gamma}x_{j,\mathrm{in}}^{B_2},\\
\dot{p}_j^{B_1} &= -\frac{\gamma}{2}p_j^{B_1} - Jx_j^{A_1} - Jx_j^{B_2} - Jx_{j+1}^{A_1} - \sqrt{\gamma}p_{j,\mathrm{in}}^{B_1},\\
\dot{p}_j^{A_2} &= -\frac{\gamma}{2}p_j^{A_2} - Jx_j^{B_2} - Jx_j^{A_1} - \sqrt{\gamma}p_{j,\mathrm{in}}^{A_2},
\end{aligned} \tag{22}$$

and $\{x_j^{A_2}, x_j^{B_1}, x_j^{A_1}, x_j^{B_2}\}$, reading

$$\begin{aligned}
\dot{x}_j^{A_2} &= -\frac{\gamma}{2}x_j^{A_2} + Jp_j^{A_1} + Jp_j^{B_2} - \sqrt{\gamma}x_{j,\mathrm{in}}^{A_2},\\
\dot{x}_j^{B_1} &= -\frac{\gamma}{2}x_j^{B_1} - Jp_j^{A_1} + Jp_j^{B_2} + Jp_{j+1}^{A_1} - \sqrt{\gamma}x_{j,\mathrm{in}}^{B_1},\\
\dot{p}_j^{A_1} &= -\frac{\gamma}{2}p_j^{A_1} - Jx_j^{A_2} - Jx_j^{B_1} - Jx_{j-1}^{B_1} - \sqrt{\gamma}p_{j,\mathrm{in}}^{A_1},\\
\dot{p}_j^{B_2} &= -\frac{\gamma}{2}p_j^{B_2} - Jx_j^{A_2} - Jx_j^{B_1} - \sqrt{\gamma}p_{j,\mathrm{in}}^{B_2}.
\end{aligned} \tag{23}$$

The fact that these two sets decouple is a consequence of the pairing we found for qNR rings. We now switch to reciprocal space, $|j\rangle \equiv \frac{1}{\sqrt{N}}\sum_k e^{-\mathrm{i}ka}|k\rangle$, in which we used Dirac notation to denote the basis vectors $\{|j\rangle\}$ and $\{|k\rangle\}$ and a mimics a lattice spacing (we set $a = 1$). We obtain two dynamical matrices for each of these sets

$$\begin{aligned}
\mathcal{M}_1(k) &= \begin{pmatrix} -\frac{\gamma}{2} & 0 & J(-1+e^{-\mathrm{i}k}) & J \\ 0 & -\frac{\gamma}{2} & J & J \\ -J(1+e^{\mathrm{i}k}) & -J & -\frac{\gamma}{2} & 0 \\ -J & -J & 0 & -\frac{\gamma}{2} \end{pmatrix},\\
\mathcal{M}_2(k) &= \begin{pmatrix} -\frac{\gamma}{2} & 0 & J & J \\ 0 & -\frac{\gamma}{2} & J(-1+e^{\mathrm{i}k}) & J \\ -J & -J(1+e^{-\mathrm{i}k}) & -\frac{\gamma}{2} & 0 \\ -J & -J & 0 & -\frac{\gamma}{2} \end{pmatrix}.
\end{aligned} \tag{24}$$

We calculate a topological invariant from each matrix, namely the winding number of their determinant

$$\nu_{1,2} = \frac{1}{2\pi\mathrm{i}}\int_0^{2\pi} \mathrm{d}k\, \det \mathcal{M}_{1,2}(k). \tag{25}$$

We find

$$\begin{aligned}
\det \mathcal{M}_{1,2}(k) = &-2J^4\cos(k) + \frac{1}{16}\left(\gamma^4 + 16J^4 + 12\gamma^2J^2\right)\\
&\pm i\left(2J^4 + \frac{\gamma^2J^2}{2}\right)\sin(k),
\end{aligned} \tag{26}$$

in which we choose the $(-)$ sign for $\det \mathcal{M}_1(k)$ and the $(+)$ sign for $\det \mathcal{M}_2(k)$. These two curves wind in opposite directions in the complex plane, as k evolves from 0 to 2π,

inducing the opposite sign for ν_1 and ν_2 (see Fig. 4 (e) in the main text).

Above, we used the plane-wave basis to identify the non-trivial topology of each block $\mathcal{M}_1(k)$, $\mathcal{M}_2(k)$. The eigenvalues of $\mathcal{M}_1(k)$ are also the eigenvalues of $\mathcal{M}_2(k)$, albeit for a different k. Together they form a degenerate sub-space. To obtain the physical (and real) eigenvectors, i.e. pairs of canonically conjugated, real valued quadratures, we need to superpose eigenvectors from these sub-spaces.

Data availability

The data in this study are available from the Zenodo repository at https://doi.org/10.5281/zenodo.XXXX.

Author contributions C.C.W. developed the theoretical framework with J.d.P. and M.B.. J.J.S. fabricated the sample, performed the experiments, and analysed the data. E.V. and A.N. supervised the project. All authors contributed to the interpretation of the results and writing of the manuscript.

Competing interests The authors declare no competing interests.

Correspondence and requests for materials should be addressed to Andreas Nunnenkamp or Ewold Verhagen.

[1] L. Deák and T. Fülöp, Reciprocity in quantum, electromagnetic and other wave scattering, Annals of Physics **327**, 1050 (2012).

[2] D. Jalas, A. Petrov, M. Eich, W. Freude, S. Fan, Z. Yu, R. Baets, M. Popovic, A. Melloni, J. Joannopoulos, M. Vanwolleghem, C. Doerr, and H. Renner, What is – and what is not – an optical isolator, Nature Photonics **7**, 579–582 (2013).

[3] C. Caloz, A. Alù, S. Tretyakov, D. Sounas, K. Achouri, and Z. Deck-Léger, Electromagnetic nonreciprocity, Phys. Rev. Applied **10**, 047001 (2018).

[4] E. Verhagen and A. Alù, Optomechanical nonreciprocity, Nature Physics **13**, 922 (2017).

[5] H.-K. Lau and A. A. Clerk, Fundamental limits and nonreciprocal approaches in non-Hermitian quantum sensing, Nature Communications **9**, 4320 (2018).

[6] L. Ranzani and J. Aumentado, Graph-based analysis of nonreciprocity in coupled-mode systems, New Journal of Physics **17**, 023024 (2015).

[7] T. Ozawa, H. M. Price, A. Amo, N. Goldman, M. Hafezi, L. Lu, M. C. Rechtsman, D. Schuster, J. Simon, O. Zilberberg, and I. Carusotto, Topological photonics, Rev. Mod. Phys. **91**, 015006 (2019).

[8] B. Abdo, F. Schackert, M. Hatridge, C. Rigetti, and M. Devoret, Josephson amplifier for qubit readout, Applied Physics Letters **99**, 162506 (2011).

[9] Z. Yu and S. Fan, Complete optical isolation created by indirect interband photonic transitions, Nature Photonics **3**, 91–94 (2009).

[10] H. Lira, Z. Yu, S. Fan, and M. Lipson, Electrically driven nonreciprocity induced by interband photonic transition on a silicon chip, Phys. Rev. Lett. **109**, 033901 (2012).

[11] A. Kamal, J. Clarke, and M. Devoret, Noiseless nonreciprocity in a parametric active device, Nature Physics **7**, 311–315 (2011).

[12] D. Malz, L. D. Tóth, N. R. Bernier, A. K. Feofanov, T. J. Kippenberg, and A. Nunnenkamp, Quantum-limited directional amplifiers with optomechanics, Phys. Rev. Lett. **120**, 023601 (2018).

[13] A. Metelmann and A. A. Clerk, Nonreciprocal photon transmission and amplification via reservoir engineering, Phys. Rev. X **5**, 021025 (2015).

[14] B. Abdo, A. Kamal, and M. Devoret, Nondegenerate three-wave mixing with the Josephson ring modulator, Phys. Rev. B **87**, 014508 (2013).

[15] K. M. Sliwa, M. Hatridge, A. Narla, S. Shankar, L. Frunzio, R. J. Schoelkopf, and M. H. Devoret, Reconfigurable josephson circulator/directional amplifier, Phys. Rev. X **5**, 041020 (2015).

[16] F. Lecocq, L. Ranzani, G. A. Peterson, K. Cicak, R. W. Simmonds, J. D. Teufel, and J. Aumentado, Nonreciprocal microwave signal processing with a field-programmable josephson amplifier, Phys. Rev. Applied **7**, 024028 (2017).

[17] J. Kim, M. C. Kuzyk, K. Han, H. Wang, and G. Bahl, Non-reciprocal Brillouin scattering induced transparency, Nature Physics **11**, 275 (2015).

[18] Z. Shen, Y.-L. Zhang, Y. Chen, C.-L. Zou, Y.-F. Xiao, X.-B. Zou, F.-W. Sun, G.-C. Guo, and C.-H. Dong, Experimental realization of optomechanically induced nonreciprocity, Nat. Photonics **10**, 657 (2016).

[19] F. Ruesink, M.-A. Miri, A. Alù, and E. Verhagen, Nonreciprocity and magnetic-free isolation based on optomechanical interactions, Nature Communications **7**, 13662 (2016).

[20] K. Fang, J. Luo, A. Metelmann, M. H. Matheny, F. Marquardt, A. A. Clerk, and O. Painter, Generalized nonreciprocity in an optomechanical circuit via synthetic magnetism and reservoir engineering, Nature Physics **13**, 465 EP (2017).

[21] G. A. Peterson, F. Lecocq, K. Cicak, R. W. Simmonds, J. Aumentado, and J. D. Teufel, Demonstration of efficient nonreciprocity in a microwave optomechanical circuit, Phys. Rev. X **7**, 031001 (2017).

[22] S. Barzanjeh, M. Wulf, M. Peruzzo, M. Kalaee, P. B. Dieterle, O. Painter, and J. M. Fink, Mechanical on-chip microwave circulator, Nature Communications **8**, 953 (2017).

[23] N. R. Bernier, L. D. Tóth, A. Koottandavida, M. A. Ioannou, D. Malz, A. Nunnenkamp, A. K. Feofanov, and T. J. Kippenberg, Nonreciprocal reconfigurable microwave optomechanical circuit, Nature Communications **8**, 604 (2017).

[24] D. B. Sohn, O. E. Örsel, and G. Bahl, Electrically driven optical isolation through phonon-mediated photonic Autler–Townes splitting, Nature Photonics **15**, 822 (2021).

[25] L. Fan, J. Wang, L. T. Varghese, H. Shen, B. Niu, Y. Xuan, A. M. Weiner, and M. Qi, An all-silicon passive optical diode, Science **335**, 447 (2012).

[26] Y.-X. Wang, C. Wang, and A. A. Clerk, Quantum nonreciprocal interactions via dissipative gauge symmetry (2022).

[27] C. Sayrin, C. Junge, R. Mitsch, B. Albrecht, D. O'Shea, P. Schneeweiss, J. Volz, and A. Rauschenbeutel, Nanophotonic optical isolator controlled by the internal state of cold atoms, Phys. Rev. X **5**, 041036 (2015).

[28] S. Buddhiraju, A. Song, G. T. Papadakis, and S. Fan, Nonreciprocal metamaterial obeying time-reversal symmetry, Phys. Rev. Lett. **124**, 257403 (2020).

[29] A. McDonald, T. Pereg-Barnea, and A. A. Clerk, Phase-dependent chiral transport and effective non-Hermitian dynamics in a bosonic Kitaev-Majorana chain, Phys. Rev. X **8**, 041031 (2018).

[30] V. P. Flynn, E. Cobanera, and L. Viola, Deconstructing effective non-Hermitian dynamics in quadratic bosonic Hamiltonians, New J. Phys. (2020).

[31] V. P. Flynn, E. Cobanera, and L. Viola, Topology by dissipation: Majorana bosons in metastable quadratic Markovian dynamics, Phys. Rev. Lett. **127**, 245701 (2021).

[32] C. C. Wanjura, M. Brunelli, and A. Nunnenkamp, Topological framework for directional amplification in driven-dissipative cavity arrays, Nature Communications **11**, 3149 (2020).

[33] S. Fan, W. Suh, and J. D. Joannopoulos, Temporal coupled-mode theory for the fano resonance in optical resonators, J. Opt. Soc. Am. A **20**, 569 (2003).

[34] C. W. Gardiner and M. J. Collett, Input and output in damped quantum systems: Quantum stochastic differential equations and the master equation, Phys. Rev. A **31**, 3761 (1985).

[35] A. A. Clerk, M. H. Devoret, S. M. Girvin, F. Marquardt, and R. J. Schoelkopf, Introduction to quantum noise,

measurement, and amplification, Rev. Mod. Phys. **82**, 1155 (2010).
[36] V. B. Braginsky, Y. I. Vorontsov, and K. S. Thorne, Quantum nondemolition measurements, Science **209**, 547 (1980).
[37] A. A. Clerk, F. Marquardt, and K. Jacobs, Back-action evasion and squeezing of a mechanical resonator using a cavity detector, New Journal of Physics **10**, 095010 (2008).
[38] M. Brunelli, D. Malz, and A. Nunnenkamp, Conditional dynamics of optomechanical two-tone backaction-evading measurements, Phys. Rev. Lett. **123**, 093602 (2019).
[39] A. Metelmann and A. A. Clerk, Quantum-limited amplification via reservoir engineering, Phys. Rev. Lett. **112**, 133904 (2014).
[40] T.-C. Chien, O. Lanes, C. Liu, X. Cao, P. Lu, S. Motz, G. Liu, D. Pekker, and M. Hatridge, Multiparametric amplification and qubit measurement with a kerr-free josephson ring modulator, Phys. Rev. A **101**, 042336 (2020).
[41] H. J. Carmichael, Quantum trajectory theory for cascaded open systems, Phys. Rev. Lett. **70**, 2273 (1993).
[42] C. W. Gardiner, Driving a quantum system with the output field from another driven quantum system, Phys. Rev. Lett. **70**, 2269 (1993).
[43] J. P. Mathew, J. d. Pino, and E. Verhagen, Synthetic gauge fields for phonon transport in a nano-optomechanical system, Nature Nanotechnology **15**, 198 (2020).
[44] J. del Pino, J. J. Slim, and E. Verhagen, Non-Hermitian chiral phononics through optomechanically induced squeezing, Nature **606**, 82 (2022).
[45] J. Koch, A. A. Houck, K. L. Hur, and S. M. Girvin, Time-reversal-symmetry breaking in circuit-QED-based photon lattices, Phys. Rev. A **82**, 043811 (2010).
[46] M. Z. Hasan and C. L. Kane, Colloquium: Topological insulators, Rev. Mod. Phys. **82**, 3045 (2010).
[47] D. Porras and S. Fernández-Lorenzo, Topological amplification in photonic lattices, Phys. Rev. Lett. **122**, 143901 (2019).
[48] Z. Gong, Y. Ashida, K. Kawabata, K. Takasan, S. Higashikawa, and M. Ueda, Topological phases of non-Hermitian systems, Phys. Rev. X **8**, 031079 (2018).
[49] Y.-X. Wang and A. A. Clerk, Non-Hermitian dynamics without dissipation in quantum systems, Phys. Rev. A **99**, 063834 (2019).
[50] A. McDonald and A. A. Clerk, Exponentially-enhanced quantum sensing with non-hermitian lattice dynamics, Nature Communications **11**, 5382 (2020).
[51] S. Barzanjeh, A. Xuereb, S. Gröblacher, M. Paternostro, C. A. Regal, and E. M. Weig, Optomechanics for quantum technologies, Nature Physics **18**, 15 (2022).
[52] J. Ningyuan, C. Owens, A. Sommer, D. Schuster, and J. Simon, Time- and site-resolved dynamics in a topological circuit, Phys. Rev. X **5**, 021031 (2015).
[53] Z. Zhang, Q. Wei, Y. Cheng, T. Zhang, D. Wu, and X. Liu, Topological creation of acoustic pseudospin multipoles in a flow-free symmetry-broken metamaterial lattice, Phys. Rev. Lett. **118**, 084303 (2017).
[54] T. M. Karg, B. Gouraud, C. T. Ngai, G.-L. Schmid, K. Hammerer, and P. Treutlein, Light-mediated strong coupling between a mechanical oscillator and atomic spins 1 meter apart, Science **369**, 174 (2020).
[55] A. Youssefi, S. Kono, A. Bancora, M. Chegnizadeh, J. Pan, T. Vovk, and T. J. Kippenberg, Topological lattices realized in superconducting circuit optomechanics, Nature **612**, 666 (2022).
[56] R. Rossignoli and A. M. Kowalski, Complex modes in unstable quadratic bosonic forms, Phys. Rev. A **72**, 032101 (2005).
[57] M. J. Weaver, F. Buters, F. Luna, H. Eerkens, K. Heeck, S. de Man, and D. Bouwmeester, Coherent optomechanical state transfer between disparate mechanical resonators, Nature Communications **8**, 824 (2017).
[58] M. Aspelmeyer, T. J. Kippenberg, and F. Marquardt, Cavity optomechanics, Rev. Mod. Phys. **86**, 1391 (2014).
[59] R. Leijssen, G. R. La Gala, L. Freisem, J. T. Muhonen, and E. Verhagen, Nonlinear cavity optomechanics with nanomechanical thermal fluctuations, Nature Communications **8**, 16024 (2017).
[60] M. Poggio, C. L. Degen, H. J. Mamin, and D. Rugar, Feedback cooling of a cantilever's fundamental mode below 5 mK, Physical Review Letters **99**, 017201 (2007).
[61] M. Rossi, D. Mason, J. Chen, Y. Tsaturyan, and A. Schliesser, Measurement-based quantum control of mechanical motion, Nature **563**, 53 (2018).
[62] B. D. Hauer, T. J. Clark, P. H. Kim, C. Doolin, and J. P. Davis, Dueling dynamical backaction in a cryogenic optomechanical cavity, Phys. Rev. A **99**, 053803 (2019).